ARTICLE

Materials and Corrosion

Influence of Al and Fe additions on metal dusting of NiCr alloys

Clara Schlereth[1] | **Ceyhun Oskay**[1] | **Heike Hattendorf**[2] |
Benedikt Nowak[2] | **Mathias C. Galetz**[1]

[1]DECHEMA-Forschungsinstitut, High Temperature Materials, Frankfurt am Main, Germany

[2]VDM Metals International GmbH, Altena, Germany

Correspondence
Clara Schlereth, DECHEMA-Forschungsinstitut, High Temperature Materials, Theodor-Heuss-Allee 25, D-60486 Frankfurt am Main, Germany.
Email: clara.schlereth@dechema.de

Abstract

Corrosion by metal dusting causes problems in various industries that process carbonaceous gases. Recently, the chromium- and aluminum-rich Ni-based Alloy 699 XA was introduced as a material with high resistance against metal dusting attacks. In this study, the metal dusting degradation of Alloy 699 XA and model alloys was investigated. In the model alloys, the aluminum, chromium, and iron contents were varied to analyze the role of each element systematically. Alloy 602 CA was included as a reference material. It was found that the alloys with the highest chromium and aluminum contents (30 and 2–3 wt%, respectively) showed the highest resistance against metal dusting. Also, the limited addition of iron enhanced the aluminum activity and thereby promoted the formation and maintenance of an aluminum-rich oxide scale. This effect at low iron levels is contrary to the negative impact of iron at higher levels, which typically leads to an increased metal dusting susceptibility. Exposure tests were performed with two gas mixtures having similar compositions, but different carbon activities. It was found that both gases had a similar aggressiveness regarding metal dusting attacks.

KEYWORDS
alloy development, gas composition, metal dusting, oxide former

1 | INTRODUCTION

Metal dusting is a high-temperature corrosion process observed in carbonaceous atmospheres at temperatures between 400°C and 800°C. These conditions are inevitable in some processes such as synthesis gas production, iron ore reduction, and methanol plants.[1–3] During the metal dusting of Ni-based alloys, carbon diffuses into the metal surface causing the sub-surface zone to become supersaturated with carbon. Then, the graphite crystallizes at the surface and grain boundaries of the alloy. The formation of graphite disintegrates the metal and vast amounts of coke with carbide, oxide, and metal particles form.[4–6]

Inhibition of metal dusting can be obtained by choosing a resistant alloy or applying a protective coating.[7–9] Unfortunately, both iron and nickel, base elements for most high-temperature alloys, catalyze the decomposition of carbon monoxide, thereby promoting the inward diffusion of carbon.[4,5] Two alloying or

---

coating approaches are currently pursued to inhibit metal dusting: (1) addition of elements inhibiting the catalytic activity of iron and nickel, such as tin or copper.[7,8,10] (2) high amounts of chromium, aluminum, and silicon are used to establish a protective oxide scale.[9,11–13]

Metal dusting resistant alloys usually contain 15–35 wt% chromium and up to 5 wt% aluminum. Chromia and alumina scales have a very low carbon solubility and act as a diffusion barrier.[14] Aluminum additions improve the protection by forming an alumina scale below the chromia scale.[15] Oxide scales formed to prevent metal dusting need to be dense, continuous, and with a low density of defects. Small physical defects such as microcracks and pores in the scale can allow the process gas access to the base metal. If the chromium and aluminum contents of the alloy are high enough, the scale can be rehealed in the case of crack formation or spallation. However, if chromium and aluminum become depleted underneath the oxide scale, rehealing becomes impossible.[16] Instead, the remaining chromium, along with iron, titanium, and niobium, can react with the gas and form carbides. Subsequently, the subsurface zone supersaturates with carbon and the metal dusting process proceeds as described above. Characteristic pits form during this type of attack on oxide-forming alloys and grow rapidly.[5,17] The pit initiation time depends on both material properties and process parameters and is difficult to estimate. Metal dusting is a catastrophic corrosion process due to this uncertainty and rapid pit growth.

Although both Fe- and Ni-based alloys with Cr and Al additions are used in metal dusting conditions, Ni-based alloys often perform better in atmospheres with low water vapor contents.[18] Among the Ni-based alloys, Alloy 693 with 29 wt% Cr and 3 wt% Al was observed to be a very resistant alloy.[12,19,20] Recently, Alloy 699 XA has been introduced as a novel alloy suitable for metal dusting environments.[21,22] This Ni-based alloy contains about 30 wt% chromium and 2 wt% aluminum which leads to a significant improvement in workability and weldability compared to Alloy 693. Like in many other Ni-based alloys, the Al additions promote the formation of γ'-phase precipitates in the alloy. In previous studies, the metal dusting behavior of Alloy 699 XA was shown to be superior to Alloy 602 CA and Alloy 690.[21] A recent study[22] on a 699 XA weld joint at 620°C showed that a protective alumina scale was obtained in fine-grained regions. On coarse-grained areas of the weld joint, a thicker chromia layer with more flaws was reported.

In the current study, the metal dusting behavior of model alloys based on the composition of 699 XA with varying chromium, aluminum, and iron contents was investigated to evaluate the optimum content of each element towards protective behavior. Additionally, the performance of the commercial Alloy 602 CA was compared to the model alloys.

Besides the oxide scale formation behavior of the alloy at very low oxygen partial pressures, the aggressiveness of the metal dusting attack is affected by the process parameters. In this study, highly aggressive conditions (compared to most industrial processes) were chosen intentionally to evaluate the alloy performance in a reasonably short timeframe. Metal dusting attack is found to be the most aggressive at temperatures between 500°C and 700°C.[3] Gases in which metal dusting occurs typically contain CO, CO_2, H_2, H_2O, and C_xH_y species. The main reactions of CO decomposition are the synthesis gas reaction (Equation 1) and the Boudouard reaction (Equation 2).[23]

$$CO(g) + H_2(g) \leftrightarrow C(s) + H_2O(g), \qquad (1)$$

$$2CO(g) \leftrightarrow C(s) + CO_2(g). \qquad (2)$$
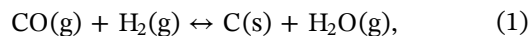
A CO/H_2 ratio around one and a gas with a high carbon activity are suitable parameters for aggressive testing conditions.[3,24,25] Additionally, it was shown that increasing pressure reduces pit initiation time.[20,26] The second objective of this study was to compare the aggressiveness of two gases with similar compositions but different carbon activities—the carbon activity of Gas 1 was double that of Gas 2.

2 | EXPERIMENTAL PROCEDURE

2.1 | Alloys

The chemical compositions of the investigated alloys are shown in Table 1. An overview of the relationship between the alloy compositions is given in Figure 1. Both commercial and laboratory-produced samples of Alloy 699 XA (named Alloy 699 XA and NiCr30Al2Fe0.5 in the following, respectively) were included. Two experiments were performed with variations in the gases. The samples of commercial Alloy 699 XA were taken from different heats: "699 XA heat A" was exposed in Gas 1, and "699 XA heat B" in Gas 2. As a reference, commercially produced Alloy 602 CA was included in both experiments.

The model alloy NiCr25Al2Fe0.5 was designed with less chromium compared to Alloy 699 XA to characterize the role of the chromium content on the metal dusting resistance. The model alloy NiCr30Fe1 with only 0.2 wt% aluminum was included to compare its metal dusting

TABLE 1 Composition of the tested material in weight percent (wt%)

Alloy (heat)	C	Cr	Ni	Mn	Si	Ti	Nb	Fe	Al	Other <0.3	Cr + Al	Cr + 3Al + 3Si	Mean grain size/μm
602 CA[a]	0.17	25.7	62.0	0.1	0.05	0.1	0.01	9.4	2.2	Zr, Y	27.9	32.5	76
NiCr25Al2Fe0.5	0.02	25.0	71.8	0.04	0.04		0.01	0.2	0.6	2.1	27.1	31.4	218
NiCr30Fe1	0.03	29.7	68.8	0.03	0.05	<0.01	0.01	1.0	0.2		29.9	30.5	92
699 XA[a] heat A	0.02	28.9	68.2	0.01	0.05		0.02	0.1	0.5	2.0 Zr	30.9	35.1	170
699 XA[a] heat B	0.02	29.5	68.0	<0.01	0.1		0.01	0.1	0.1	2.1 Zr	31.6	36.0	83
NiCr30Al2Fe0.5	0.02	29.6	67.4	0.04	0.05	<0.01	0.2	0.4	2.2		31.8	36.4	161
NiCr30Al2Fe2	0,02	28,9	66,7	0,04	0,05	0,01	0,16	2,0	2,1		31,0	35,4	229
NiCr30Al2Fe4	0.02	29.5	63.9	0.04	0.04		0.01	0.15	4.2	2.1 Zr	31.6	35.9	124
NiCr30Al3Fe2.5	0.02	29.5	63.4	0.04	0.04	0.4	0.6	2.7	3.2	Zr	32.7	39.2	198

[a]Commercial molten, otherwise laboratory melts, S < 0.005, N ≤ 0.03, p < 0.01, B < 0.005, V ≤ 0.03, Cu ≤ 0.01, Co < 0.05, Mo < 0.05, W < 0.02; chromium equivalents and mean grain sizes before exposure; measurement uncertainty of 0.2 wt%.
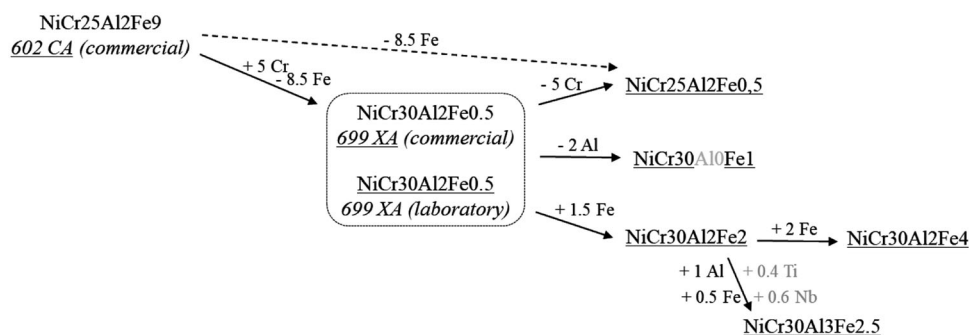

FIGURE 1 Overview of the relationship between the tested commercial and model alloys. The terms used in the article are underlined. For detailed compositions see Table 1

resistance with alloys with more aluminum and analyze the influence of aluminum on the scaling behavior. To investigate the influence of iron additions, the model alloys NiCr30Al2Fe2, NiCr30Al2Fe4 and Ni-Cr30Al3Fe2.5 were included. NiCr30Al2Fe2 and Ni-Cr30Al2Fe4 have a higher iron content than Alloy 699 XA, but the same aluminum and chromium content. NiCr30Al3Fe2.5 additionally has a slightly higher aluminum level to investigate the combined effect of the two elements.

In several studies on the alloying contents for metal dusting resistant materials, a chromium equivalent [9,11,27–29] was postulated as a practical parameter to indicate the metal dusting resistance of the alloy with various threshold values described by different authors. A summary of chromium equivalents is given in Table 2. In Table 1, in addition to the composition, the combined chromium plus aluminum content[9] and the Schillmoller chromium equivalent[11] are given for each alloy.

All alloys were produced by VDM Metals GmbH. The commercial alloys were hot-formed to final thickness, solution annealed, and mill ground. The laboratory alloys of about 10 kg were hot-formed to final thickness and solution annealed. The blanks for the test coupons were sawed and milled down to around 5 mm to obtain homogeneous bulk material. All samples were then machined with wire-cutting and the surfaces were ground down to P500 grit (all main, side, and edge surfaces). The final dimensions of the samples were precisely determined using an electronic caliper and were around 15 mm × 10 mm. Mean grain sizes were measured by the linear intercept method (see Table 1).

TABLE 2 Chromium equivalents necessary for metal dusting resistant alloys according to various studies

Postulated condition, contents in wt%	Reference
$Cr_{equiv} = Cr + 2 \times Si > 24$	[27]
High Cr_{equiv} with $Cr_{equiv} = Cr + 3 \times (Si + Al)$	[11]
Cr > 28 in Ni-based alloys	[28]
Cr + Al > 33	[9,29]
low Fe content	[39,40]

2.2 | Metal dusting exposure and analytical characterization

Exposure tests were conducted in a test rig equipped for high-pressure tests. One sample of each alloy was placed in separate alumina crucibles in a horizontal tube furnace (tube material: Centralloy® ET 45 Micro). A detailed description of the testing equipment was given previously.[26] To reduce the oxygen content in the furnace before exposure, it was flushed with argon (with max. 2 ppm oxygen) overnight before the exposure. Then, the furnace was heated to 620°C under sustained Ar flow with a volumetric rate of 3.6 L/h. Once 620°C was achieved, the test gas was released into the furnace and the pressure was increased up to 19 bar. The gas flow was set to a linear rate of 0.96 cm/min at the samples. Table 3 shows the compositions of the two test gases. The table also provides the carbon activity of the unreacted gas mixtures according to the synthesis gas or Boudouard reaction and the estimated oxygen partial pressure in thermodynamic equilibrium, calculated with the Software FactSage 6.1.[30] At these oxygen partial pressures, the formation of alumina and chromia is expected, while Fe- and Ni-oxides are unstable. Discontinuous isothermal tests were conducted for intervals of 125 or 250 h, adding up to a total exposure time of 750 h in Gas 1 and 1000 h in Gas 2. Exposure tests were ended by first decreasing the pressure, flushing with argon, and then cooling down the furnace. Samples were cleaned in an ultrasonic bath with water and ethanol after each exposure. The net specific mass change was determined using a precision (0.01 mg) weighing balance (Mettler-Toledo). For the samples exposed in Gas 2, Raman spectroscopy (Renishaw inVia Raman Microscope) was conducted at laser wavelengths of 532 and 633 nm to characterize the oxide scales of the samples. Cross-sections of these samples were prepared using conventional metallographic methods including galvanic Ni-plating, grinding up to P1200 grit SiC paper, and polishing down to 1 μm using diamond suspensions. Some of the cross-sections were etched using V2A etchant at 50°C to observe the alloy microstructure underneath the oxide scales. Electron probe microanalysis (EPMA) was used to generate high resolution backscattered electron images and elemental distribution maps with a spatial resolution of about 0.5 μm.

3 | RESULTS

The specific net mass change kinetics of the cleaned samples are shown in Figure 2. High mass losses were found for alloys 602 CA, NiCr25Al2Fe0.5 and NiCr30Fe1 during exposure to both gases. For better comparison, mass losses after 750 h are shown in Figure 3. Correspondingly, these same alloys also showed the most intense pitting attack, as shown in the macroimages in Figures 4 and 5. Pit initiation started during the first 500 h for all samples. On the more resistant samples, fewer pits formed. Pit diameter growth rates were determined for each sample by measuring the diameters of up to five pits per sample. The average growth rates, projected to mm per year, are shown in Figure 6. However, on some samples, mass loss is caused by the growth of a few pits, others showed new pit formation during the entire exposure. This formation of new pits, for example, on Alloy 602 CA, NiCr25Al2Fe0.5, or NiCr30Fe1, is reflected in the mismatch of the mass loss and the measured growth rates of individual pits. Most samples showed slightly faster pit growth rates in Gas 1. A particularly higher mass loss in Gas 1 compared to Gas 2 was observed for Alloy 602 CA and NiCr25Al2Fe0.5. In Gas 1 most alloys had fewer, but larger, pits than in Gas 2 (see Figures 4 and 5).

Comparison of Alloy 699 XA and its laboratory alloy NiCr30Al2Fe0.5 with the model alloy NiCr25Al2Fe0.5 shows that the lower chromium content led to a dramatic increase in mass loss and the number of pits in Gases 1 and 2. Reduction of the aluminum content from 2.1 wt% in 699 XA to 0.2 wt% in NiCr30Fe1 also resulted in an increase in mass loss and the number of pits (only tested in Gas 2, see Figures 3 and 5). The comparison of the three NiCr30Al2Fe alloys with different iron contents was done very carefully, because of the above-mentioned marked influence of the chromium content. This is about 0.6% lower in NiCr30Al2Fe2 than in NiCr30Al2Fe0.5 and NiCr30Al2Fe4. NiCr30Al2Fe2 shows a higher mass loss and more pits in Gas 1 than NiCr30Al2Fe0.5 and NiCr30Al2Fe4. Mass loss and pit formation of NiCr30Al2Fe4 is lower than of NiCr30Al2Fe0.5 (see Figure 3).

For the laboratory alloys, the pit density was higher on the sides than on the main surfaces (see Figures 4 and 5). This may be due to different levels of impurities

	Composition (vol%)				Carbon activity a_c		
	CO	H$_2$O	CO$_2$	H$_2$	CO reduction	Boudouard	pO$_2$ (bar)
Gas 1	49	1	2	48	1351	1442	3.4×10^{-23}
Gas 2	47	2	4	47	634	663	3.5×10^{-23}

TABLE 3 Composition and carbon activity of the initial gases and oxygen partial pressure at thermodynamic equilibrium (calculated with FactSage 6.1) at 620°C and 19 bar pressure
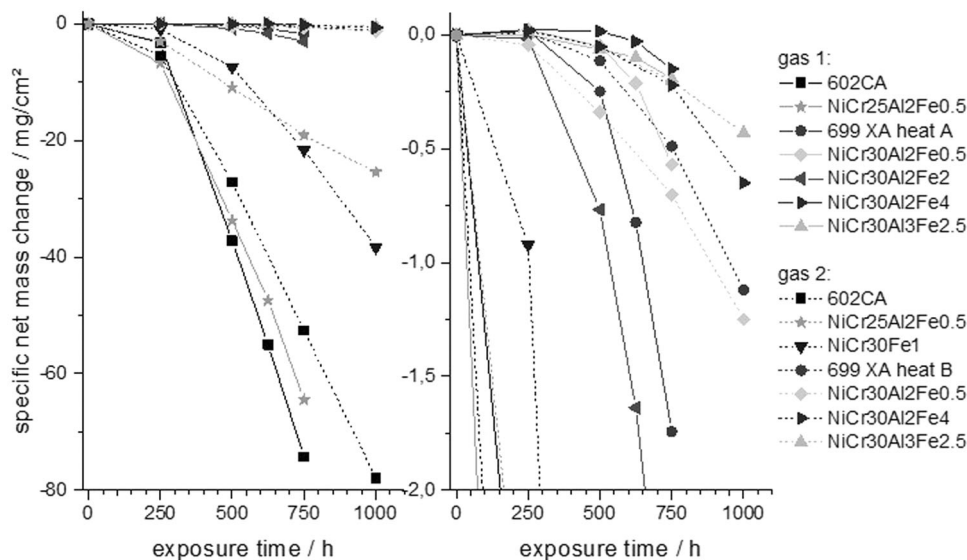
FIGURE 2 Specific net mass change kinetics of the samples during exposure tests in both gas mixtures (please refer to Table 3 for the gas compositions). Please note that the right diagram is an enlarged Y-axis view of the left diagram
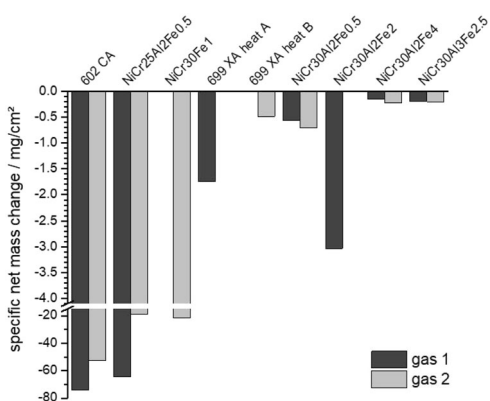

FIGURE 3 Specific net mass losses of the samples after exposure for 750 h. NiCr30Fe1 was only exposed in Gas 2 and NiCr30Al2Fe2 was only exposed in Gas 1

from the melting and casting of the low volume laboratory melts. Hence, upon comparing the metal dusting resistance of the laboratory alloys to commercial alloys, solely considering the mass loss can be misleading. The mass loss kinetics should be considered together with the metallographic and analytical characterization to evaluate the overall metal dusting resistance of the laboratory alloys.

Typical metal dusting pits are composed of coke, a carbon enriched zone, and a carburized zone. In a previous study on Alloy 699 XA, it was shown that the carbon-enriched zone contains lamellar Cr_3C_2 precipitates in a chromium-depleted austenite matrix.[22] In the carburized zone, carbon is dissolved in the matrix. Figure 7a shows a cross-sectional view of a pit formed within Alloy 602 CA. Alloy 602 CA

contains chromium-rich carbide precipitates, which are introduced into the material to improve its creep strength.[31] Figure 7b shows a pit formed in Alloy 699 XA heat B. Underneath the pit surface, a carburized zone and a carbon-enriched zone can be distinguished. The rapid pit growth in Alloy 602 CA (Figure 6) and lack of a carbon-enriched zone (Figure 7a) indicate that its carburized zone is transformed into coke directly.

The carbon ingress in the pits of model alloys is shown for NiCr30Fe1 and NiCr30Al2Fe4 in Figure 8. Based on those images the C-enriched zone is markedly thicker than the carburized zone in the pit of NiCr30Fe1 compared to NiCr30Al2Fe4. From the cross-sections of the samples exposed in Gas 2, it was observed that NiCr30Fe1 and NiCr30Al2Fe4, as well as Alloy 699 XA heat B, show similar structures of the C-enriched and carburized zones in the pit. However, the C-enriched zone is thinner for NiCr30Al2Fe4 compared to the other alloys.

The element distributions of the pit and nonattacked surface, exemplified for Alloy 699 XA heat B, are shown in Figures 9 and 10. The carburized zone has a thickness of $11 \pm 6\,\mu m$ for Alloy 699 XA heat B. Below the carburized zone, chromium carbides formed along the grain boundaries. In all cross-sections, no carbon is detected underneath the nonattacked oxide scale. The chemical composition of the thin oxide scales could not be determined with EPMA due to spatial resolution limitations.

Raman spectroscopy was used to determine the oxide phases at the surfaces. Exemplified Raman spectra are given in Figure 11 and assigned phases of the samples are
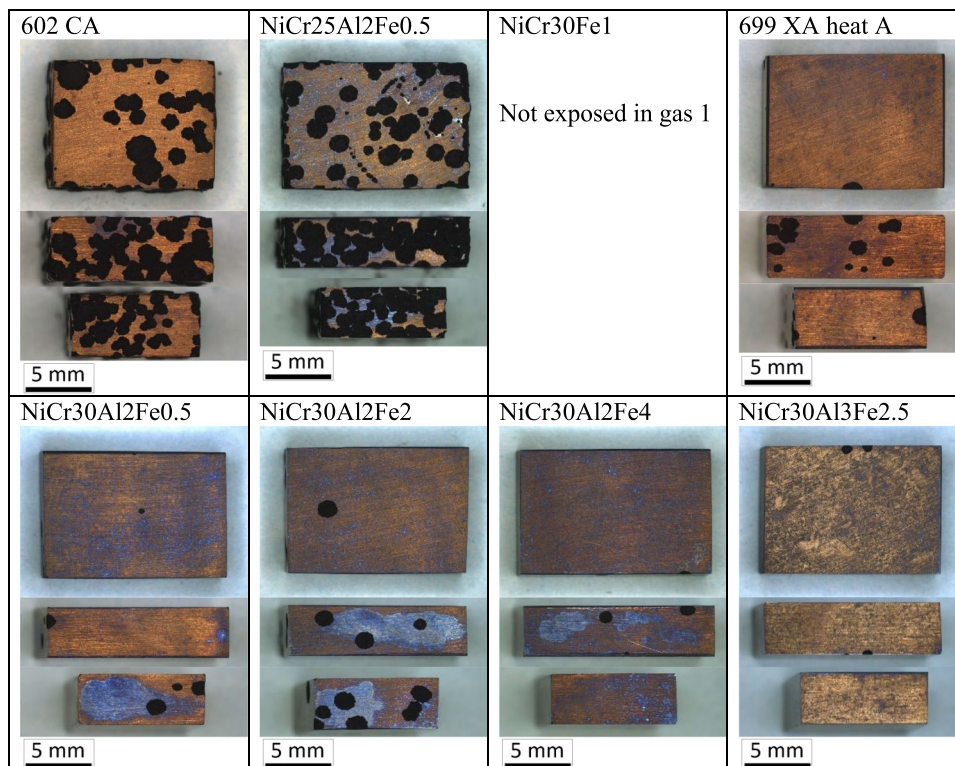
FIGURE 4 Macroimages of samples after 750 h exposure in Gas 1 [Color figure can be viewed at wileyonlinelibrary.com]
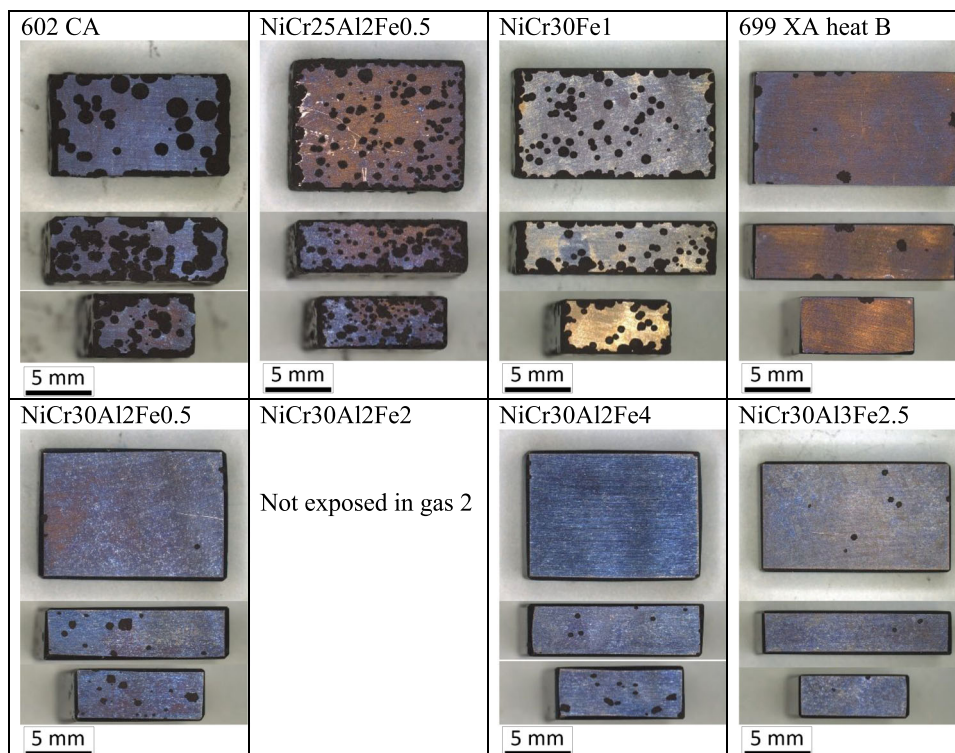

FIGURE 5 Macroimages of samples after 750 h exposure in Gas 2 [Color figure can be viewed at wileyonlinelibrary.com]
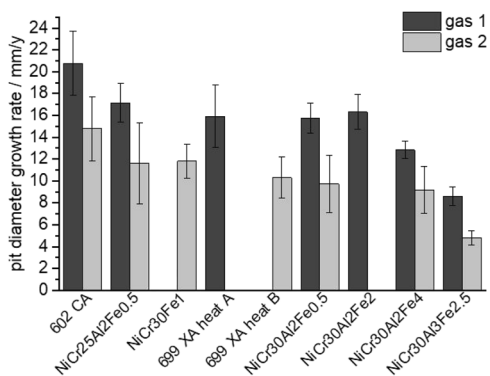
FIGURE 6 Pit diameter growth rate of all alloys during exposure

listed in Table 4. The scales were found to consist mainly of chromia[32] and to a lower extent α-alumina,[33] depending on the alloy composition. Glassy carbon[34] was detected on all samples as well. On NiCr25Al2Fe0.5, NiCr30Al2Fe0.5, and NiCr30Al2Fe4, more than 100 measurements with 633 nm laser wavelength were performed, all of them showed the strong presence of α-alumina. Although transformation from γ- to α-alumina during oxidation in gases with high oxygen contents is expected at temperatures around 900°C,[35,36] formation of α-alumina at 620°C is unusual, but has been reported in other metal dusting literature.[37–39] Only the samples of 602 CA, NiCr30Al3Fe2.5, and NiCr30Fe1 show additional weak peaks around Raman shifts of 690–720 cm^{-1}. These are characteristic for various spinel phases, for example, Ni(Fe, Cr)$_2$O$_4$.[32]

4 | DISCUSSION

Commercial and laboratory Ni-based alloys with compositions derived from Alloy 699 XA were exposed to harsh environments causing metal dusting attacks on all

samples. Possible factors affecting the aggressivity of attack are the Cr, Al, and Fe content as well as the grain size and gas composition.

4.1 | Influence of chromium and aluminum content

Comparing the tested alloys regarding the sum of chromium and aluminum content (chromium equivalent proposed by Hermse et al.),[9,29] the value varied between 27.1 and 32.7 wt%. In general, the samples with fewer pits had a higher chromium equivalent (calculated according to Hermse et al.[9] or Parks et al.[11]) than the other alloys (see Figures 4 and 5). Hermse et al.[9] postulated that the sum should be larger than 33 wt% to give a metal dusting resistant alloy, this condition is not fulfilled for any of the investigated alloys (see Tables 1 and 3). The Schillmoller chromium equivalent of all investigated alloys was larger than the critical value of 24 wt% according to Schillmoller.[27] The mass change kinetics (see Figure 2) and the macroimages (see Figures 4 and 5) show that this value is not sufficient to provide a high resistance against metal dusting for the test conditions used in this study. Another rule on the minimum element content was postulated by Röhnert et al.,[28] claiming chromium contents above 28 wt% in Ni-based alloys are necessary to protect the alloy. This is in line with the observed metal dusting attack for the samples of 602 CA and NiCr25Al2Fe0.5, both with only 25 wt% chromium. However, the intense pit formation on NiCr30Fe1 compared to other samples with 30 wt% chromium is unpredicted by Röhnert's 28 wt% thresholds. NiCr30Fe1 has a reduced aluminum content of only 0.2 wt%, supporting the theory that aluminum is necessary to inhibit carbon ingress and has a much stronger impact than chromium, as
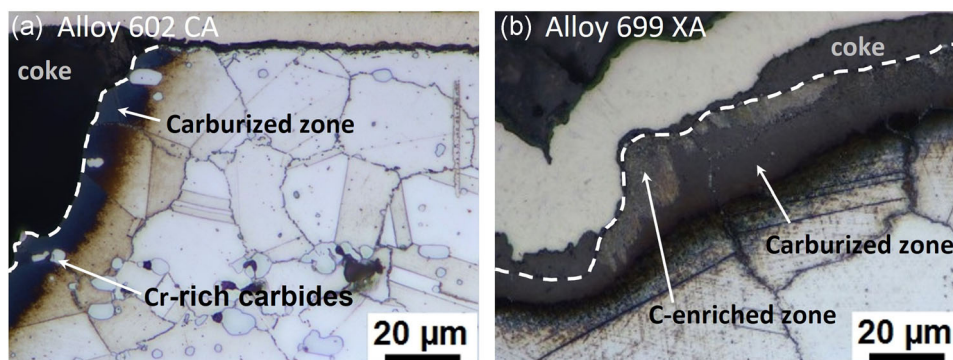

FIGURE 7 Optical microscope images of etched cross-sections after 1000 h exposure in Gas 2, the dotted line represents the metal/coke interface in the pit, (a) alloy 602 CA, (b) Alloy 699 XA heat B [Color figure can be viewed at wileyonlinelibrary.com]
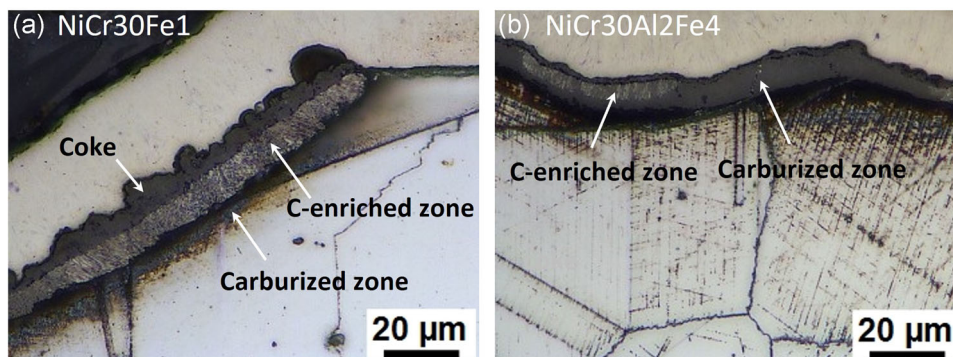
FIGURE 8 Optical microscope images of etched cross-sections after 1000 h exposure in Gas 2, (a) NiCr30Fe1, (b) NiCr30Al2Fe4 [Color figure can be viewed at wileyonlinelibrary.com]
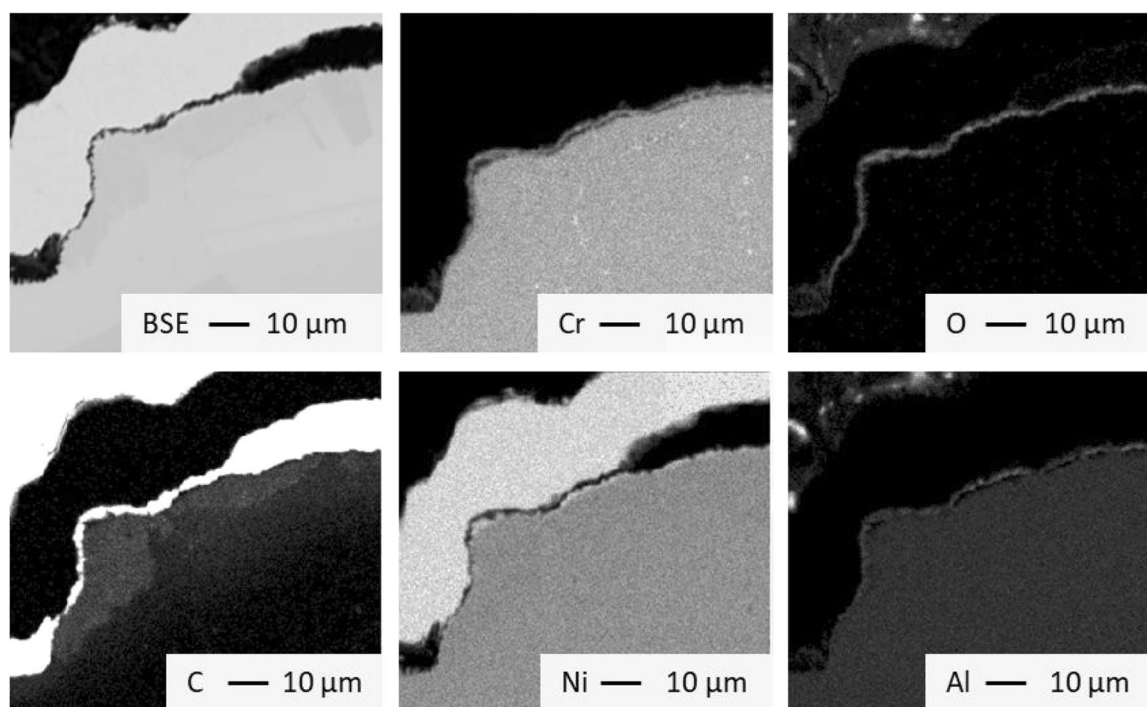

FIGURE 9 Element distribution maps (EPMA) in a pit within Alloy 699 XA heat B after 1000 h in Gas 2. EPMA, electron probe microanalysis

long as it can form a continuous and dense scale.[15] Chen et al.[19] studied the metal dusting behavior of 699 XA (acquired from the same batch as the 699 XA heat B sample exposed to Gas 1 in this study) under the same conditions denoted as Gas 2 in this study. They showed that a continuous alumina scale formed below the external chromia scale. In general, higher amounts of chromium and aluminum are expected to improve the metal dusting resistance through the formation of a protective oxide scale with the capability to reheal defects.

4.2 | Considerations of minor differences in chromium content and grain size

The model alloys with varied iron content (NiCr30Al2Fe) had a slightly higher mass loss in Gas 2, while the Alloy 699 XA heat A sample showed a higher mass loss in Gas 1. This may be due to the lower chromium content of 28.9 wt% in Alloy 699 XA heat A compared to 29.5 wt% in Alloy 699 XA heat B. The Alloy 699 XA heat A also had a larger grain size of 170 µm compared to 83 µm for Alloy
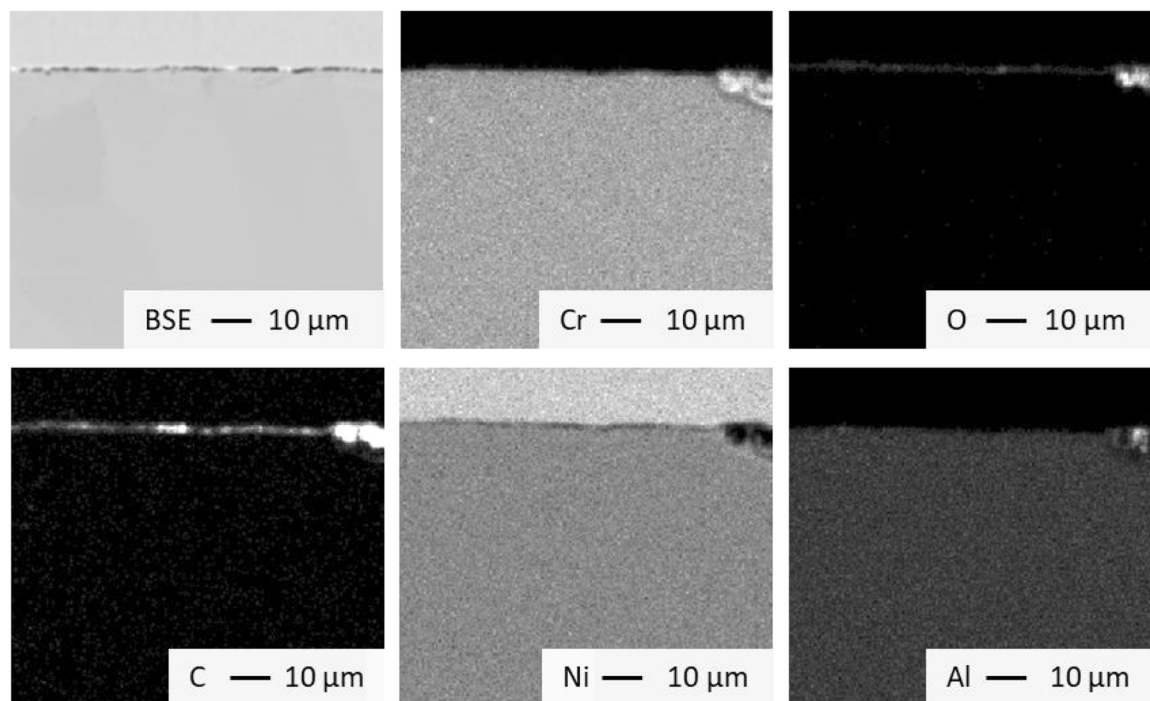
FIGURE 10 Element distribution (EPMA) next to a pit within Alloy 699 XA heat B after 1000 h in Gas 2. EPMA, electron probe microanalysis
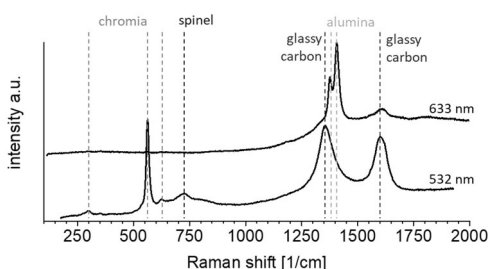

FIGURE 11 Exemplified Raman spectra of samples containing alumina and glassy carbon, obtained with a laser wavelength of 633 nm, or chromia, spinel, and glassy carbon, obtained with a laser wavelength of 532 nm

TABLE 4 Signal intensity of oxide phases detected with Raman spectroscopy on samples after 1000 h exposure in Gas 2

Alloy	Chromia	Spinel	Alumina
602 CA	Strong	Weak, at 701 cm^{-1}	Weak
NiCr25Al2Fe0.5	Strong	None	Strong
NiCr30Fe1	Strong	Weak, at 690 cm^{-1}	None
699 XA heat B	Strong	None	Weak
NiCr30Al2Fe0.5	Strong	None	Strong
NiCr30Al2Fe4	Strong	None	Strong
NiCr30Al3Fe2.5	Strong	Weak, at 718 and 726 cm^{-1}	Weak

699 XA heat B. Larger grains correlate with fewer grain boundaries and thus slower chromium diffusion for the formation and rehealing of the oxide scale. The outward diffusion of chromium and thus the rehealing properties of the chromia scale is determined both by the actual chromium content and the grain size. However, the chromium reservoir in the grains is high and the chromium depletion below the oxide scale is negligible (as determined with EPMA, not shown). A study of Hattendorf et al.[40] showed that on Alloy 601 (22.8 wt% chromium), the metal dusting attack did not differ between samples with smaller (13 μm) and larger (267 μm) grains after 1955 h exposure at 600°C and 20 bar in a 37% CO, 7% CO$_2$, 46% H$_2$, 9% H$_2$O atmosphere. Therefore, the grain boundary area is not decisive for the resistance of high-Cr alloys. Instead, the impact of surface deformation by grinding was found to be more decisive for the outward diffusion of chromium in this temperature range.[41] In the case of industrial applications, where mechanical loads are superimposed with a chemical attack, the grain size is expected to play a bigger role in the interaction between mechanical and chemical damage mechanisms.

Among the NiCr30Al2Fe model alloys, NiCr30Al2Fe2 has a lower chromium content of 28.9 wt% and showed a higher mass loss and more pits when compared to NiCr30Al2Fe0.5 and NiCr30Al2Fe4 with 29.6 or 29.5 wt% Cr, respectively (see Figures 3 and 4) in Gas 1. In the
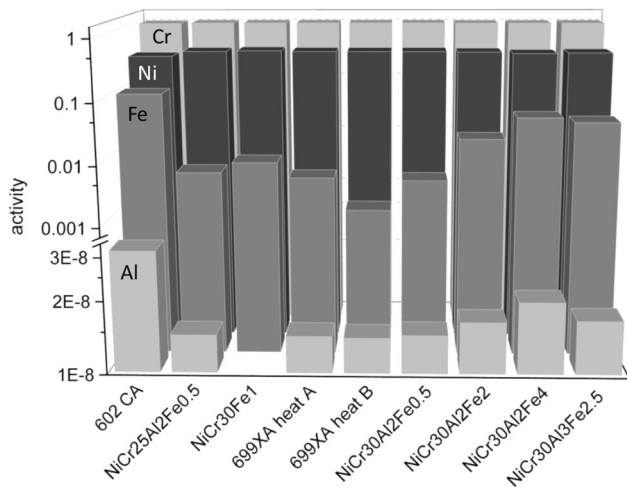
FIGURE 12 Activities of aluminum, chromium, nickel, and iron in the alloys were calculated with JMatPro (MatPlus GmbH). Please note the break in the y-axis. Displayed aluminum activities are in the range of 1.4×10^{-8}–3.2×10^{-8}, the aluminum activity of NiCr30Fe1 is 2.2×10^{-9}. Iron, nickel, and chromium activities are higher than 8×10^{-4}

FIGURE 13 Phase distribution at thermodynamic equilibrium at 620°C as calculated with JMatPro

tested aggressive conditions, it is assumed that the threshold for chromium supply was not reached with the NiCr30Al2Fe2 sample in Gas 1. Due to the minor difference in chromium content with a seemingly strong impact, the NiCr30Al2Fe2 sample was not included in the analysis of the influence of the iron content. The similar chromium contents of NiCr30Al2Fe0.5, NiCr30Al2Fe4, and NiCr30Al3Fe2.5 allowed first considerations on the effect of iron additions.

4.3 | Influence of the iron content

As a catalyst for CO decomposition, reduction of the iron content can reduce the susceptibility to metal dusting.[12,15,39,40] Surprisingly, the addition of 4.2 wt%

TABLE 5 Calculated aluminum content in the γ- and γ′-phase in wt% at equilibrium

Al in wt%	In the alloy	γ-Phase	γ′-Phase
602 CA	2.20	1.67	8.09
NiCr25Al2Fe0.5	2.10	1.23	7.74
699 XA heat A	2.00	1.23	7.66
699 XA heat B	2.10	1.21	7.60
NiCr30Al2Fe0.5	2.20	1.21	7.65
NiCr30Al2Fe2	2.10	1.30	7.77
NiCr30Al2Fe4	2.10	1.41	7.90
NiCr30Al3Fe2.5	3.20	1.25	7.86

iron slightly increased the metal dusting resistance when comparing alloys NiCr30Al2Fe0.5 and NiCr30Al2Fe4. This is likely associated with variations in aluminum activities. The activities of nickel, iron, chromium, and aluminum in the alloys were calculated with the software JMatPro (MatPlus GmbH) and are given in Figure 12. Note that the aluminum activities are all in the range of 10^{-8} while the chromium, nickel, and iron activities are in the range of 10^{-4}–1. Despite the similar aluminum contents, for example, in NiCr30Al2Fe0.5, NiCr30Al2Fe2, and NiCr30Al2Fe4, the alloys have different aluminum activities. According to equilibrium calculations with JMatPro, 82–86 at% of the aluminum content is present in the γ′-phase in all alloys, except for NiCr30Fe1, which does not exhibit the γ′-phase. Between 1 and 2 wt% Al remains in the γ-phase, see Table 5. The distribution of the phases in thermodynamic equilibrium, calculated with JMatPro, is given in Figure 13. NiCr30Al3Fe2.5 contains the highest amount with 33 at% of γ′-phase. Here, the formation of γ′-phase is enhanced additionally by the titanium and niobium additions. In the other alloys, the γ′-phase varies between 10 and 18 at%. However, no γ′ precipitates are visible in the EPMA images. In a transmission electron microscopy study, an alloy with similar composition had γ′ precipitates in the nm range after 100 h exposure at 800°C.[42] Precipitates formed after 1000 h at 620°C are expected to be in the same size range and cannot be resolved with EPMA due to the spatial resolution limit of 1 μm. The composition of the γ′-phase in at% is given in Table 6. In alloys with iron additions, the amount of iron in the γ′-phase is also increased. According to Albers et al.[43] and Elano et al.,[44] substituting Fe for Ni in the γ′-phase can result in an increased Al activity. Up to a certain iron content, the negative influence of iron as the catalyst for the CO decomposition can be probably outweighed by its positive effect on the aluminum activity and therefore the formation of a dense alumina subscale. In our study, the increased aluminum activity led to higher resistance against metal dusting attacks for the NiCr30Al3Fe2.5 and

TABLE 6 Composition of the γ'-phase calculated by JMatPro

In at%	Ni	Al	Cr	Fe	Mn	Nb	Si	Ti
602 CA	71.85	15.89	8.42	2.32	0.07	0.05	0.11	1.02
NiCr25Al2Fe0.5	72.91	15.31	10.74	0.14	0.02	0.75	0.06	0.08
699 XA heat A	72.84	15.14	11.06	0.11	0.00	0.54	0.08	0.15
699 XA heat B	72.77	15.01	11.45	0.03	0.00	0.47	0.14	0.07
NiCr30Al2Fe0.5	72.81	15.12	11.13	0.10	0.02	0.62	0.16	0.03
NiCr30Al2Fe2	72.67	15.35	10.62	0.50	0.025	0.60	0.082	0.07
NiCr30Al2Fe4	72.47	15.61	9.82	1.09	0.03	0.62	0.07	0.08
NiCr30Al3Fe2.5	73.37	15.58	7.63	0.71	0.03	1.05	0.08	1.37

the NiCr30Al2Fe4 samples. Raman spectroscopy showed the presence of alumina scales on all samples except NiCr30Fe1. Further investigation is necessary to characterize the alumina scales in detail.

4.4 | Pit growth

Apart from the mass loss, the pit growth rates gave valuable information towards estimating the time to failure of the alloys. Analysis of the pit diameter growth (Figure 6) gave different rates depending on the alloy composition. This implies that not only the time to pit initiation but also the pit growth rate, depends on the alloy composition.

4.5 | Role of the gas composition

Samples were exposed to two gas mixtures with different carbon activities and slightly varied compositions. A higher mass loss in the gas with the higher carbon activity was found for Alloy 602 CA. This effect was even more pronounced for NiCr25Al2Fe0.5, the two alloys with the most intense pitting (see Figure 3). For the other alloys tested in both gases, mass losses do not differ significantly between the gases. For the alloys in Gas 1 fewer, but larger pits developed in comparison to Gas 2, and a higher pit growth rate in Gas 1 is detected for all alloys (see Figure 3). This may relate to the higher carbon activity of Gas 1, but more tests are necessary to determine the detailed correlation between the pit characteristics and the gas composition. The more pronounced growth of single pits would be detrimental for applications. In general, the difference in metal dusting attack in the gases is not as large as the carbon activities might suggest and a detailed look at the gas compositions and carbon activities gives an explanation. The carbon activities were calculated individually for

synthesis gas (Equation 3) or Boudouard reactions (Equation 4):

$$a_{C(1)} = K_{(1)} \frac{p_{CO}\, p_{H_2}}{p_{H_2O}} \tag{3}$$

$$a_{C(2)} = K_{(2)} \frac{p_{CO}{}^2}{p_{CO_2}} \tag{4}$$

where $K_{(1)}$ and $K_{(2)}$ are the equilibrium constants for the synthesis gas and Boudouard reaction, respectively. A higher carbon activity was achieved in this study by reducing the amount of CO_2 and H_2O. However, the amounts of CO and H_2 of both gases are only slightly changed. The thermodynamic equilibria of the gases at the exposure conditions were calculated with FactSage 6.1.[30] The gas compositions at thermodynamic equilibrium are similar. As the gas flows through the furnace, it will not only contact the samples, but also the furnace tube and the alumina crucibles containing the samples. Reactions of the gases at these surfaces can change their compositions towards thermodynamic equilibrium. It can be postulated that the dwell time in the furnace is long enough to allow slight compositional changes of the gases resulting in converging carbon activities. Hence, the behavior of the samples in both gases does not differ significantly, even though the carbon activities of the initial gases might suggest the opposite.

5 | CONCLUSION

This study investigated the metal dusting behavior of model alloys based on the composition of Alloy 699 XA at 620°C and 19 bar. The findings of the study can be summarized as follows:

Larger mass losses and higher pit growth rates were found for alloys with 25 wt% instead of 30 wt% of chromium (Alloy 602 CA and NiCr25Al2Fe0.5) as well

as 0.2 wt% instead of 2 wt% aluminum (NiCr30Fe1). Low differences in the chromium content between 28.9 and 29.5 wt% could play a decisive role in the resistance against aggressive atmospheres, highlighting the important role of the Cr level.

Samples with around 29.5 wt% Cr, more than 2 wt% Al and additions of low amounts of iron (2.7 wt% or 4.2 wt%) had slightly increased resistance against metal dusting. This may be explained by the change in aluminum activity. Substitution of Ni with Fe in the γ′-phase increases the aluminum activity and may thus promote the formation of an even more protective oxide scale. This may compensate for the increased metal dusting susceptibility through the increasing Fe content up to a certain level of iron. Although the limited samples here suggest this mechanism, an alloy series designed for this specific question needs to be investigated to test the hypothesis.

Exposure tests were performed with two gas mixtures. Despite the large difference in carbon activity of the initial gases, the specific net mass losses of the samples were unexpectedly similar. The gases had similar compositions at equilibrium and it is theorized they react in the furnace towards thermodynamic equilibrium in the hot zone, resulting in converging carbon activities.

DATA AVAILABILITY STATEMENT
The data that support the findings of this study are available from the corresponding author upon reasonable request.

ORCID
Clara Schlereth https://orcid.org/0000-0002-5770-782X
Ceyhun Oskay https://orcid.org/0000-0001-7504-0160
Heike Hattendorf https://orcid.org/0000-0002-8609-0910
Mathias C. Galetz http://orcid.org/0000-0001-6847-2053

REFERENCES
[1] H. J. Grabke, M. Spiegel, *Mater. Corros.* **2003**, *54*, 799.
[2] E. Slevolden, J. Z. Albertsen, F. U. Tjeldbergodden, in *Proc. Corros. 2011*, NACE, Houston, TX **2011**.
[3] J. J. Hoffman, M. Lin, W. R. Watkins, S. W. Dean, in *Proc. Corros. 2009*, NACE, Houston, TX **2009**.
[4] H. J. Grabke, in *Corrosion by Carbon and Nitrogen: Metal Dusting, Carburisation and Nitridation (EFC 41)* (Eds: H. J. Grabke, M. Schütze), Woodhead Publishing, Cambridge **2007**, pp. 1–24.
[5] D. J. Young, J. Zhang, C. Geers, M. Schütze, *Mater. Corros.* **2011**, *62*, 7.
[6] J. Zhang, D. J. Young, *Corros. Sci.* **2007**, *49*, 1496.
[7] C. Geers, M. Schütze, *ECS Trans.* **2009**, *25*, 71.
[8] S. Madloch, M. C. Galetz, C. Geers, M. Schütze, *Surf. Coat. Technol.* **2016**, *299*, 29.
[9] C. G. Hermse, H. van Wortel, in *Proc. Corros. 2009*, NACE, Houston, TX **2009**.
[10] Y. Nishiyama, K. Moriguchi, N. Otsuka, T. Kudo, *Mater. Corros.* **2005**, *56*, 806.
[11] S. B. Parks, C. M. Schillmoller, *Hydrocarbon Process.* **1997**, 93.
[12] B. A. Baker, G. D. Smith, in *International Workshop on Metal Dusting* (Special Metals Technical Paper), ANL, Argonne, IL, September 26–28 **2001**.
[13] A. Agüero, M. Gutiérrez, L. Korcakova, T. Nguyen, B. Hinnemann, S. Saadi, *Oxid. Met.* **2011**, *76*, 23.
[14] I. Wolf, H. J. Grabke, *Solid State Commun.* **1985**, *54*, 5.
[15] K. Natesan, Z. Zeng, in *Proc. Corros. NACE International, Houston*, **2005**.
[16] M. Schütze, in Ref. Module Mater. Sci. Mater. Eng. (Ed: S. Hashmi), Elsevier, Oxford **2016**, pp. 1–31.
[17] A. Fabas, D. Monceau, S. Doublet, A. Rouaix-Vande Put, *Corros. Sci.* **2015**, *98*, 592.
[18] A. Rouaix-Vande Put, K. A. Unocic, M. P. Brady, B. A. Pint, *Corros. Sci.* **2015**, *92*, 58.
[19] C. G. Hermse, H. van Wortel, in Metal dusting: a relation between alloy composition and degradation rate, *Proc. of Eurocorr*, DECHEMA e.V, Edinburgh. Frankfurt am Main **2008**.
[20] K. Natesan, Z. Zeng, *Development of Materials Resistant to Metal Dusting Degradation*, U.S. Department of Energy **2006**.
[21] H. Hattendorf, A. Lópes, J. Kloewer, in *Proc. Corros. 2018*, NACE, Houston, TX **2018**.
[22] W.-T. Chen, B. Li, B. Gleeson, M. C. Galetz, H. Hattendorf, in *Proc. Corros. 2019*, NACE, Houston, TX **2019**.
[23] D. J. Young, *High Temperature Oxidation and Corrosion of Metals*, Elsevier, Oxford **2008**.
[24] E. M. Müller-Lorenz, H. J. Grabke, *Mater. Corros.* **1999**, *50*, 614.
[25] C. Hermse, in *Proc. Corros. 2011*, NACE,Houston, TX **2011**, p. 11148.
[26] S. Madloch, A. Soleimani-Dorcheh, M. C. Galetz, *Oxid. Met.* **2017**, *89*, 483.
[27] C. M. Schillmoller, *Chem. Eng.* **1986**, *93*, 83.
[28] D. Röhnert, M. Schütze, T. Weber, in *Corros. 2007 Conf. Expo,* NACE, Nashville **2007**, p. 7417.
[29] C. G. Hermse, J. C. van Wortel, *Corros. Eng., Sci. Technol.* **2009**, *44*, 182.

[30] C. W. Bale, E. Bélisle, P. Chartrand, S. A. Decterov, G. Eriksson, A. E. Gheribi, K. Hack, I.-H. Jung, Y.-B. Kang, J. Melançon, A. D. Pelton, S. Petersen, C. Robelin, J. Sangster, P. Spencer, M.-A. van Ende, *Calphad* **2016**, *54*, 35.

[31] A. Chyrkin, W. G. Sloof, R. Pillai, T. Galiullin, D. Grüner, L. Singheiser, W. J. Quadakkers, *Mater. High Temp.* **2015**, *32*, 102.

[32] B. D. Hosterman, *Dissertation*, University of Nevada (Las Vegas) **2011**.

[33] V. K. Tolpygo, D. R. Clarke, *Mater. High Temp.* **2000**, *17*, 59.

[34] Z. Zeng, K. Natesan, V. A. Maroni, *Oxid. Met.* **2002**, *58*, 147.

[35] D. P. Renusch, *PhD Thesis*, Wesstern Michigan University (Kalamazoo) **1999**.

[36] H. J. Grabke, *Intermetallics* **1999**, *7*, 1153.

[37] J. Z. Albertsen, O. Grong, J. C. Walmsley, R. H. Mathiesen, W. van Beek, *Metall. Mater. Trans. A* **2008**, *39*, 1258.

[38] M. C. Galetz, C. Schlereth, E. M. White, *Mater. Corros.* **2021**, *72*, 1232.

[39] B. Li, B. Gleeson, W.-T. Chen, H. Hattendorf, in *Proc. Corros. 2020*, NACE, Houston, TX **2020**.

[40] H. Hattendorf, C. G. Hermse, R. M. IJzerman, *Mater. Corros.* **2019**, *70*, 1385.

[41] T. Gheno, C. Desgranges, L. Martinelli, *Corros. Sci.* **2020**, *173*, 108805.

[42] S. Khan, J. B. Singh, A. Verma, *Mater. Charact.* **2016**, *119*, 24.

[43] M. Albers, D. Kath, K. Hilpert, *Metall. Trans. A* **1996**, *27*, 3569.

[44] L. Eleno, K. Frisk, A. Schneider, *Intermetallics* **2006**, *14*, 1276.